Electronic Supplementary Information (ESI)

Identifying the intrinsic active site in bimetallic Co_3S_4/Ni_3S_2 feathers on MXene nanosheets as heterostructure for efficient oxygen evolution reaction

Yang Li,[a] Qi-Xuan Du,[a] Jian Cui,[a] Xiao Chen,[c] Hong-Wei Yang,*[,a] and Hua Qian*[,a,b]

[a] School of Chemistry and Chemical Engineering, Nanjing University of Science and Technology, Nanjing 210094, China

[b] China National Quality Inspection Testing Center for Industrial Explosive Materials Nanjing, 210094, China

[c] College of Environmental and Chemical Engineering, Jiangsu University of Science and Technology, Zhenjiang 212100, China

E-mail: hyang@njust.edu.cn (H. W. Yang)

Email: qianhua@njust.edu.cn (H. Qian)

Section 1. Materials and structural characterization

Nickel foam (NF) was purchased from Suzhou Sinero Technology Co., Ltd. Hexadecyl trimethyl ammonium bromide ($CH_3(CH_2)_{15}NBr(CH_3)_3$, CTAB, 98%) was obtained from Shanghai Haohong Biomedical Technology Co., Ltd. Ti_3AlC_2 MAX powder (400 mesh) was got from FoShan XinXi Technology Co., Ltd. Lithium fluoride (LiF, 99.9%), hydrochloric acid (HCl, 37 wt %), nickel (II) nitrate hexahydrate ($Ni(NO_3)_2{\cdot}6H_2O$, 99%), Cobalt (II) nitrate hexahydrate ($Co(NO_3)_2{\cdot}6H_2O$, 99.99%), urea

(NH_2CONH_2, 99%), sodium sulfide nonahydrate ($Na_2S{\cdot}9H_2O$, 99%) and ethanol were gained from Sinopharm Chemical Reagent Co., Ltd. All chemicals were purchased commercially and used as received without further purification.

Powder X-ray diffraction (PXRD) patterns were obtained on a Bruker D8 Advance X-ray diffractometer using Cu-Kα radiation (λ = 1.5418 Å). The working voltage was 40 kV and the working current was 40 mA. The patterns were collected with a 2θ range from 10° to 80° at a step of 0.0167°. X-ray photoelectron spectroscopy (XPS) of samples was gained using a Thermo ESCALAB 250XI with aluminum Kα radiation. Scanning electron microscopy (SEM) images were obtained on a Hitachi S-4800 SEM at 5 kV. The pictures of the samples were characterized by using a field emission scanning electron microscopy (FE-SEM, Hitachi S-4800 SEM) and a transmission electron microscopy (TEM, JEOL JEM200CX, JEOL). Elemental mapping was studied via high-angle annular dark-field scanning TEM energy dispersive X-ray spectroscopy (EDS).

Section 2. Electrochemical measurement

The electrochemical measurements were carried out in 1M KOH aqueous solution with a three-electrode configuration on a CORRTEST CS2350H working station at room temperature. Hg/HgO saturated with KOH and Pt filament were used as reference and counter electrodes respectively. The prepared samples with a size of 1 cm × 1 cm were directly used as the working electrodes without using any binder or conductive agent. The electrochemical impedance spectroscopy (EIS) tests were recorded in a frequency

range from 100 kHz to 0.01 Hz with 10 mV amplitude at stable open circuit voltage. The double-layer capacitances (C_{dl}) of the catalysts were determined in the non-faradaic potential region at various scan rates of (10, 25, 50, 75, and 100 $mV \cdot s^{-1}$) between 0.92 and 0.98 V vs. RHE as the means for estimating the electrochemical surface area (ECSA). The double-layer capacitance was then carried out by plotting the $\Delta J = (J_a - J_c)$ at 0.95 V vs. RHE against the scan rate. The OER activities of all the electrocatalysts were assessed by the linear sweep voltammetry (LSV) method within the potential range of 0.85-2.00 V vs. RHE. And the stability tests were performed by 1000 cyclic voltammetry (CV) cycles and the chronoamperometry (CA) measurements for 24 hours at the current density of 100 mA cm^{-2}.

Section 3. Computational method

In this manuscript, to further quantify the change of reaction free energy during water electrolysis, we performed density functional theory (DFT) calculations. All the calculations have been carried out with the Quickstep module in the CP2K v7.1 software.[1] To be more specific, all the structures have performed geometry optimization calculations under DZVP-MOLOPT-SR-GTH basis sets[2] and Geodecker–Teter–Hutter pseudopotentials Perdew-Burke-Ernzerhof (PBE) functional.[3-5] The frequency calculation is performed at the same computational level to ensure that the geometry optimization calculation structures have no imaginary frequency and obtained the free energy correction. In order to avoid the basis set superposition error (BSSE) caused by the gaussian basis group, TZVP-MOLOPT-SR-GTH has been used to obtain single-

point energy. We used DFT-D3 dispersion [6,7] to correct the scheme and note that the 400 Ry absolute energy cutoff and a 55 Ry relative cutoff have been used in all calculations.

Section 4. Construction models

To begin with, based on the XRD and HRTEM results, the Co_3S_4 (111) surface and Ni_3S_2 (110) surface slab were used to model the active surface. For Co_3S_4 crystal, the crystal surface structure is transformed as follows to ensure the lattice vectors of the (111) surface are orthogonal. The total structure extends two layers along the Y axis, and a thickness of 20 Å vacuum was added in the Y axis direction perpendicular to the slabs, which means the entire molecular model is placed into one $6.5726 \times 11.3841 \times 35.4287\ \text{Å}^3$ periodic cell (84 atoms) so that the interactions between the slab and any adjusting molecules can be eliminated.

$$Co_3S_4\ inital\ model = Co_3S_4(111)\begin{pmatrix}1 & 0 & 0\\ 1 & 2 & 0\\ 0 & 0 & 2\end{pmatrix}$$

In the Co_3S_4(111) active surface model as shown in Figure S4, the bottom 10 layers of atoms are fixed when performing a geometry optimization task (The dotted red line in Figure S4). And note that when performing the frequency calculation, the entire active catalyst layer is fixed while allowing only the adsorbed molecules to rotate.

The catalyst Ni_3S_2(110) active surface is shown in Figure S6, the crystal surface structure is transformed as follows. Like the Co_3S_4(111) surface, a thickness of 20 Å vacuum was added in the Y axis direction perpendicular to the slabs. The entire structure is placed into one $11.547 \times 8.24514677 \times 32.812\ \text{Å}^3$ periodic cell, which

contains 100 atoms. The bottom 6 layers of atoms are fixed when performing a geometry optimization task (The dotted red line in Figure S6).

$$Ni_3S_2\ inital\ model = Ni_3S_2(110)\begin{pmatrix} 2 & 0 & 0 \\ 0 & 2 & 0 \\ 0 & 0 & 4 \end{pmatrix}$$

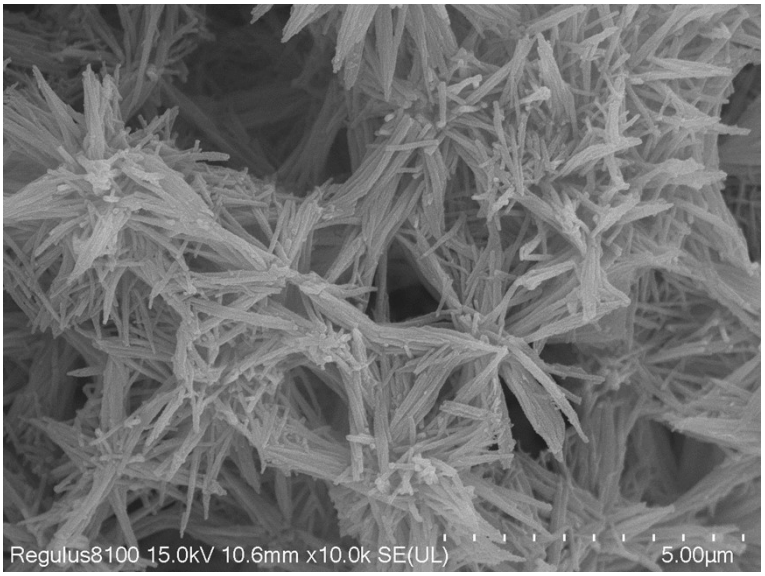

Fig. S1 The SEM image of NF@Co_3S_4/Ni_3S_2.

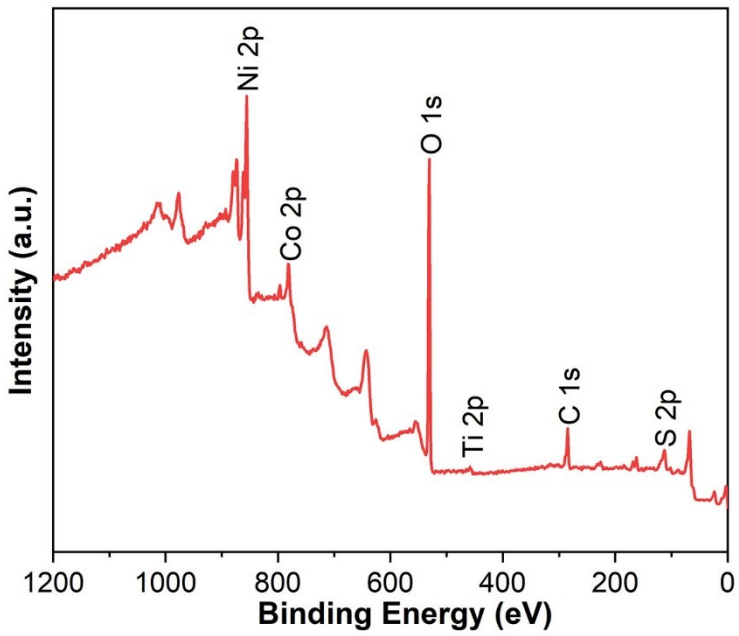

Fig. S2. XPS survey spectra of NF@MXene@Co_3S_4/Ni_3S_2.

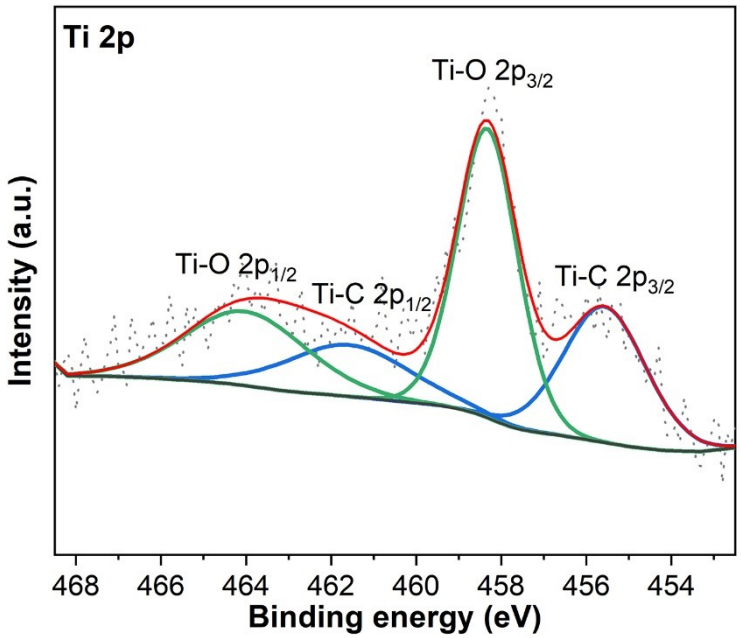

Fig. S3. High-resolution XPS spectra of Ti for NF@MXene@Co_3S_4/Ni_3S_2.

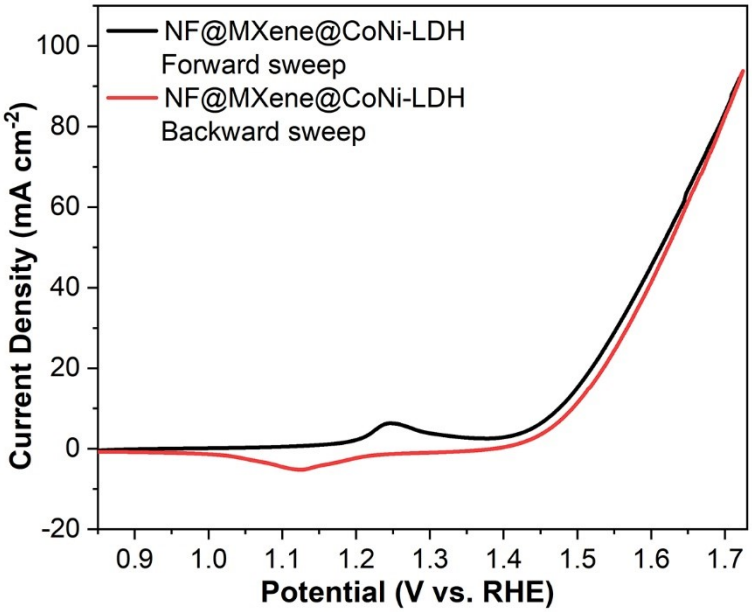

Fig. S4. Forward and backward sweep OER LSV curves of NF@MXene@CoNi-LDH.

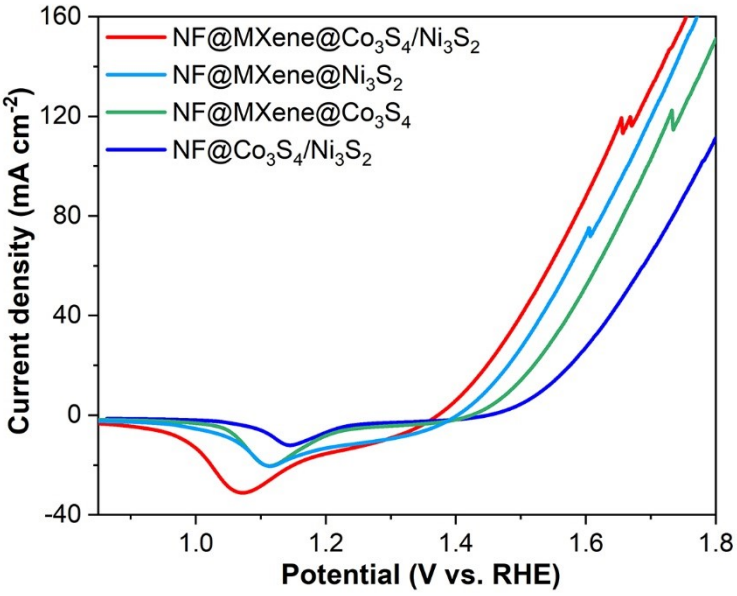

Fig. S5. LSV curves of NF@MXene@Co_3S_4/Ni_3S_2, NF@MXene@Co_3S_4, NF@MXene@Ni_3S_2 and NF@Co_3S_4/Ni_3S_2.

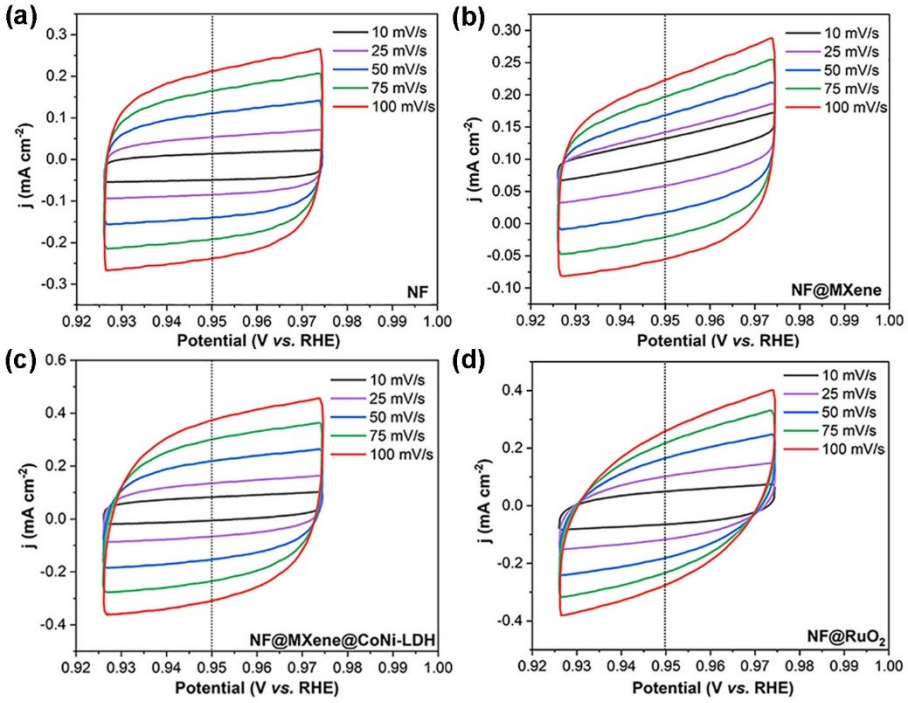

Fig. S6. CV curves at the non-faradaic potential for NF, NF@MXene, NF@MXene@CoNi-LDH and NF@RuO_2.

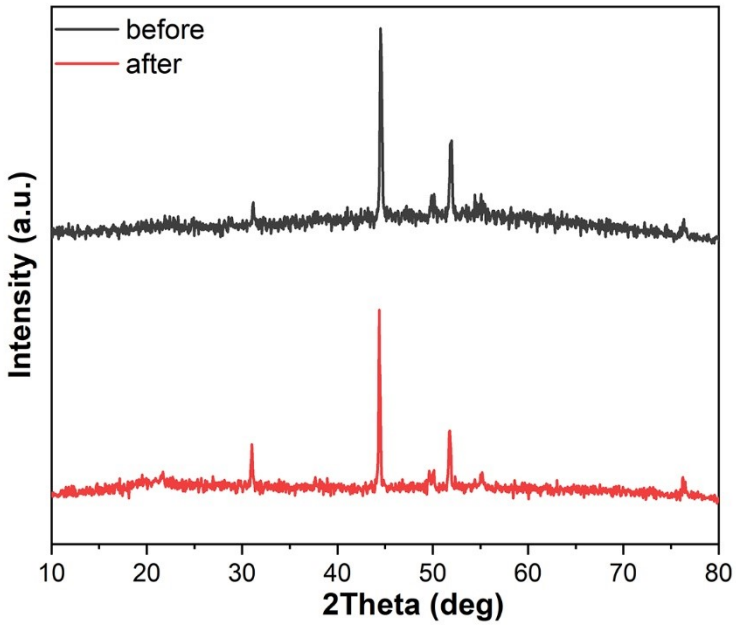

Fig. S7. PXRD patterns of NF@MXene@Co_3S_4/Ni_3S_2 before and after stability test.

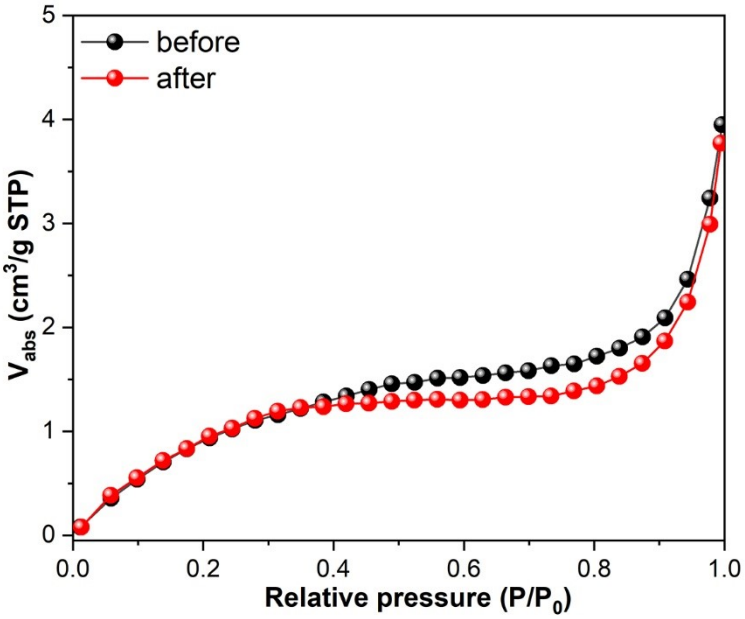

Fig. S8. Nitrogen adsorption isotherms at 77 K of NF@MXene@Co_3S_4/Ni_3S_2 before and after stability test.

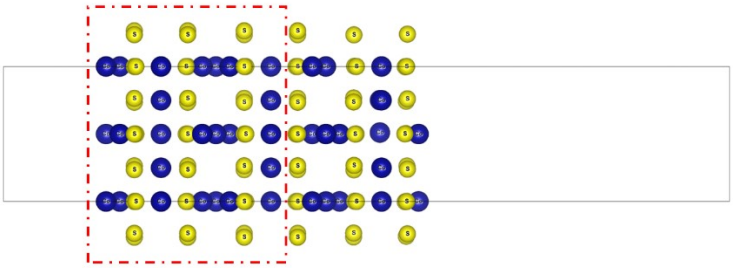

Fig. S9. Co_3S_4 (111) active surface

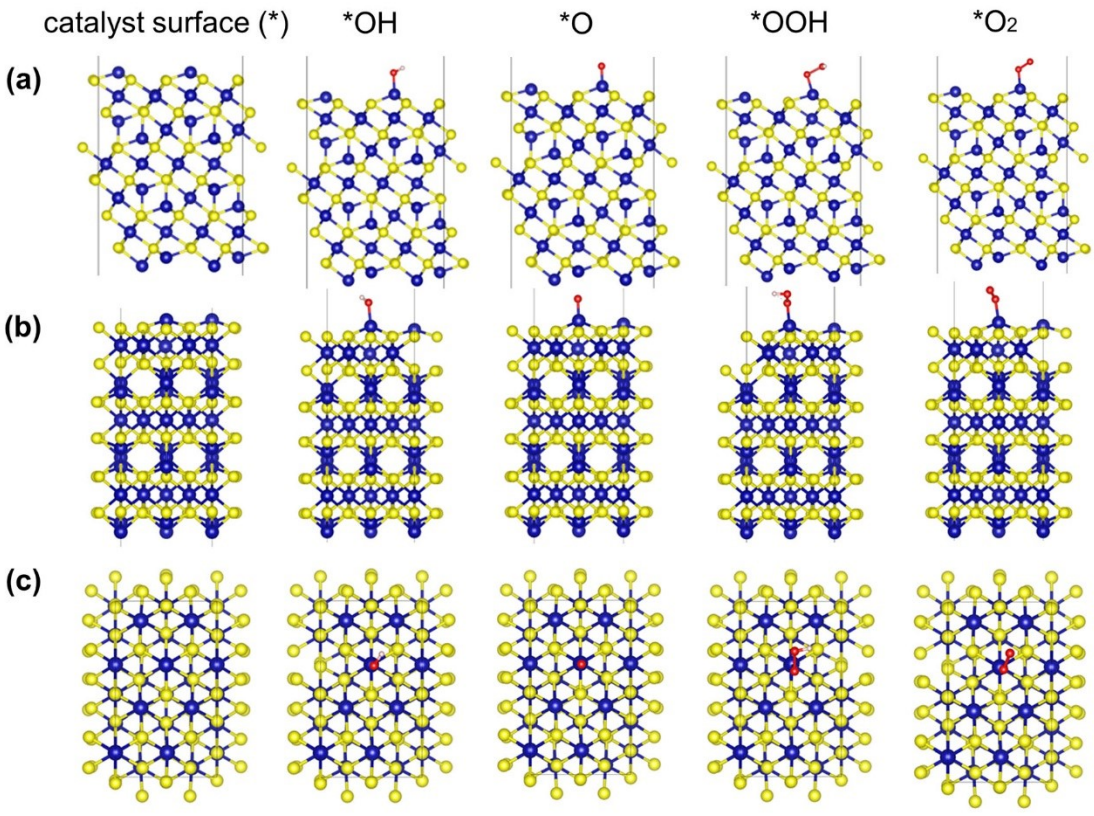

Fig. S10. Illustration of the OER reaction coordinates of Co_3S_4 (111) from (a) Front view, (b) left view and (c) top view.

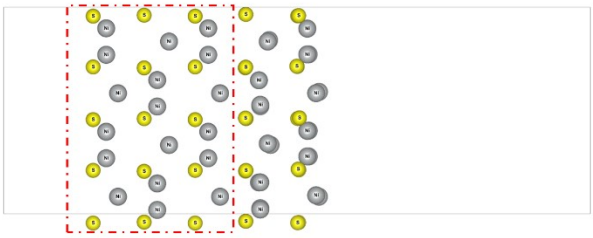

Fig. S11. Ni_3S_2 (110) active surface

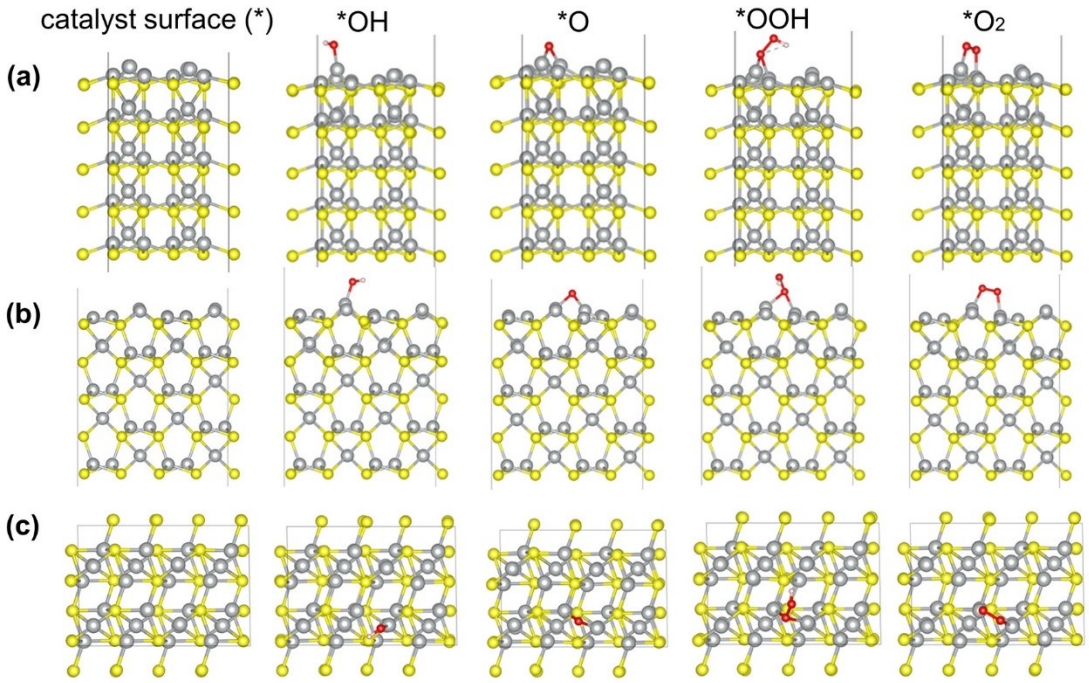

Fig. S12. Illustration of the OER reaction coordinates of Ni_3S_2 (110) from (a) Front view, (b) left view and (c) top view.

Table S1. The comparison of the electrocatalytic performance of previously reported catalysts.

Catalyst	Substrate	η_{10} (mV)	Tafel Slope (mV dec^{-1})	Ref.
NF@MXene@Co_3S_4/Ni_3S_2	NF	186	97	This work
NiCo-UMOFNs	GC	250	42	8
Co_4Ni_1P	RDE	245	61	9
Ni_3S_4	GC	307	67	10
Co_9S_8@TDC	GC	330	86	11
Ni_3S_2/Co_3S_4@PPy/NF	NF	207	52	12
$CoNi_2S_4$@CoS_2/NF	NF	259	45	13
Ni-Co_3S_4-2	GC	298	90	14
Ni_3S_2/NF	NF	296	65	15
CoS_x@Cu_2MoS_4-MoS_2/NSG	GC	351	62	16
$CoFe_{0.2}S_x$	GC	304	49	17
3D $CoS_{0.46}P_{0.54}$	GC	302	67	18
NiCo LDH/NiCoS	CC	207	48	19
NiAl-LDHs	CFP	190	60	20
NiCo LDHs	GP	249 (η_{20})	108	21
MIM-CoFe LDH	NF	217	58	22

Notes: 1M KOH, 10 mA cm^{-2}, NF-Ni foam, GC-glassy carbon, RDE-rotating disk electrode, CC-carbon cloth, CFP- carbon fiber paper, GP-graphite paper.

Table S2. BET surface area of NF@MXene@Co_3S_4/Ni_3S_2 before and after catalysis.

NF@MXene@Co_3S_4/Ni_3S_2	**BET surface area (m^2 g^{-1})**
Before catalysis	4.74
After catalysis	4.26

Table S3. Summary of the calculated free energy change of corresponding active sites during OER.

active sites	**ΔG_1 (eV)**	**ΔG_2 (eV)**	**ΔG_3 (eV)**	**ΔG_4 (eV)**	**$\Delta G_{desorp.}$ (eV)**
Co_3S_4	0.37	1.39	1.64	1.52	0.45
Ni_3S_2	0.60	1.23	1.60	1.49	0.77

Note: $\Delta G_{desorp.}$ means the free energy from $*O_2$ to O_2.

References

1. T. D. Kuhne, M. Iannuzzi, M. Del Ben, V. V. Rybkin, P. Seewald, F. Stein, T. Laino, et al, CP2K: An electronic structure and molecular dynamics software package-quickstep: efficient and accurate electronic structure calculations, *J. Chem. Phys.*, 2020, **152**, 194103.

2. J. VandeVondele and J. Hutter, Gaussian basis sets for accurate calculations on molecular systems in gas and condensed phases, *J. Chem. Phys.*, 2007, **127**, 114105.

3. S. Goedecker, M. Teter and J. Hutter, Separable dual-space gaussian pseudopotentials, *Phys. Rev. B*, 1996, **54**, 1703-1710.

4. C. Hartwigsen, S. Goedecker and J. Hutter, Relativistic separable dual-space gaussian pseudopotentials from H to Rn, *Phys. Rev. B*, 1998, **58**, 3641-3662.

5. M. Krack, Pseudopotentials for H to Kr optimized for gradient-corrected exchange-correlation functionals, *Theor. Chem. Acc.*, 2005, **114**, 145-152.

6. S. Grimme, J. Antony, S. Ehrlich and H. Krieg, A consistent and accurate ab initio parametrization of density functional dispersion correction (DFT-D) for the 94 elements H-Pu, *J. Chem. Phys.*, 2010, **132**, 154104.

7. S. Grimme, S. Ehrlich and L. Goerigk, Effect of the damping function in dispersion corrected density functional theory, *J. Comput. Chem.*, 2011, **32**, 1456-1465.

8. S. Zhao, Y. Wang, J. Dong, C.-T. He, H. Yin, P. An, K. Zhao, X. Zhang, C. Gao, L. Zhang, J. Lv, J. Wang, J. Zhang, A. M. Khattak, N. A. Khan, Z. Wei, J. Zhang, S. Liu, H. Zhao and Z. Tang, Ultrathin metal-organic framework nanosheets for electrocatalytic oxygen evolution, *Nature Energy*, 2016, **1**, 16184-16194.

9. L. Yan, L. Cao, P. Dai, X. Gu, D. Liu, L. Li, Y. Wang and X. Zhao, Metal-organic frameworks derived nanotube of nickel-cobalt bimetal phosphides as highly efficient electrocatalysts for overall water splitting, *Adv. Funct. Mater.*, 2017, **27**, 1703455.

10. K. Wan, J. Luo, C. Zhou, T. Zhang, J. Arbiol, X. Lu, B. W. Mao, X. Zhang and J. Fransaer, hierarchical porous Ni_3S_4 with enriched high-valence Ni sites as a robust electrocatalyst for efficient oxygen evolution reaction, *Adv. Funct. Mater.*, 2019, **29**, 1900315.

11. J.-Y. Zhao, R. Wang, S. Wang, Y.-R. Lv, H. Xu and S.-Q. Zang, Metal-organic framework-derived Co_9S_8 embedded in N, O and S-tridoped carbon nanomaterials as an efficient oxygen bifunctional electrocatalyst, *J. Mater. Chem. A*, 2019, **7**, 7389-7395.

12. Y. Song, P. Hong, T. Li, G. Ma, Q. Deng, Y. Zhou and Y. Zhang, A nanoflower-like polypyrrole-based cobalt-nickel sulfide hybrid heterostructures with electrons migration to boost overall water splitting, *J. Colloid Interf. Sci.*, 2022, **618**, 1-10.

13. R. Huang, W. Chen, Y. Zhang, Z. Huang, H. Dai, Y. Zhou, Y. Wu and X. Lv, Well-designed cobalt-nickel sulfide microspheres with unique peapod-like structure for overall water splitting, *J. Colloid. Interf. Sci.*, 2019, **556**, 401-410.

14. B. Yang, C. Gu, Q. Zhao, G. Zhou, L. Xu and H. Pang, Reactive template-engaged synthesis of Ni-doped Co_3S_4 hollow and porous nanospheres with optimal electronic modulation toward high-efficiency electrochemical oxygen evolution, *Inorg. Chem. Front.*, 2022, **9**, 3924-3932.

15. L. Li, C. Sun, B. Shang, Q. Li, J. Lei, N. Li and F. Pan, Tailoring the facets of Ni_3S_2 as a bifunctional electrocatalyst for high-performance overall water-splitting, *J. Mater. Chem. A*, 2019, **7**, 18003-18011.

16. D. C. Nguyen, D. T. Tran, T. L. L. Doan, D. H. Kim, N. H. Kim and J. H. Lee, Rational Design of core@shell structured CoS_x@Cu_2MoS_4 Hybridized MoS_2/N,S-codoped graphene as advanced electrocatalyst for water splitting and Zn-Air battery, *Adv. Energy Mater.*, 2020, **10**, 1903289.

17. M. Wang, C.-L. Dong, Y.-C. Huang and S. Shen, Operando spectral and

electrochemical investigation into the heterophase stimulated active species transformation in transition-metal sulfides for efficient electrocatalytic oxygen evolution, *ACS Catal.*, 2020, **10**, 1855-1864.

18. R. Boppella, J. Park, H. Lee, G. Jang and J. Moon, Hierarchically structured bifunctional electrocatalysts of stacked core-shell $CoS_{1-x}P_x$ heterostructure nanosheets for overall water splitting, *Small Methods*, 2020, **4**, 2000043.

19. J. Li, L. Wang, H. He, Y. Chen, Z. Gao, N. Ma, B. Wang, L. Zheng, R. Li, Y. Wei, J. Xu, Y. Xu, B. Cheng, Z. Yin, and D. Ma, Interface construction of NiCo LDH/NiCoS based on the 2D ultrathin nanosheet towards oxygen evolution reaction, *Nano Res.*, 2022, **15**, 4986-4995.

20. Y. Wang, Y. Liu, M. Zhang, B. Liu, Z. Zhao and K. Yan, One-step architecture of bifunctional petal-like oxygen-deficient NiAl-LDHs nanosheets for high-performance hybrid supercapacitors and urea oxidation, *Sci. China Mater*., 2022, **65**, 1805-1813.

21. C. Ye, L. Zhang, L. Yue, B. Deng, Y. Cao, Q. Liu, Y. Luo, S. Lu, B. Zheng, and X. Sun, A NiCo LDH nanosheet array on graphite felt: an efficient 3D electrocatalyst for the oxygen evolution reaction in alkaline media, *Inorg. Chem. Front.*, 2021, **8**, 3162-3166.

22. L. Hu, L. Tian, X. Ding, X. Wang, X. Wang, Y. Qin, W. Gu, L. Shi, and C. Zhu, p -d hybridization in CoFe LDH nanoflowers for efficient oxygen evolution ectrocatalysis, *Inorg. Chem. Front.*, 2022, **9**, 5296-5304.